Acta Acustica 2024, **8**, 37

https://doi.org/10.1051/aacus/2024039

Available online at:
https://acta-acustica.edpsciences.org

TECHNICAL & APPLIED ARTICLE OPEN ACCESS

The potential of additively manufactured porous absorbers in the design of multi-layer microperforated absorbers

Benedikt Berchtenbreiter*, Andreas Renz, and Stefan Becker

Friedrich-Alexander-University (FAU) Erlangen-Nuremberg, Institute of Fluid Mechanics, Cauerstr. 4, 91058 Erlangen, Germany

Received 18 April 2024, Accepted 18 July 2024

Abstract – Microperforated absorbers (MPA) are a well-established technology for attenuating sound in flow carrying ducts. MPAs usually consist of a microperforated panel (MPP) in combination with a cavity as back volume. The damping maxima of MPAs occur in the range of their resonant frequencies and the effect is narrowband compared to porous or fibrous absorbers, which damp broadband at high frequencies. The resonant frequencies of MPAs decrease with increasing back volume. This provides a challenge, especially in applications with limited installation space when the damping of low frequencies is required. In the literature, the combination of MPPs and porous or fibrous absorbers is reported to reduce the required back volume. Therefore, double-layer MPAs with an additively manufactured porous absorber underneath the MPP are introduced in this work. The advantage of using additively manufactured porous absorbers as an acoustic metamaterial over conventional absorbers is that the acoustic properties can be specifically adapted to the required impedance boundary conditions. The results of this work show that the additively manufactured absorbers reduce the required back volume by up to 13% compared with liners without absorber underneath the MPP. Experimental validation underscores the robustness of the chosen design approach for double-layer MPAs.

Keywords: Microperforated absorber (MPA), Acoustic liner, Acoustic metamaterial, Additively manufactured porous absorber, Microperforated panel (MPP)

1 Introduction

The design of sound-absorbing liners in flow carrying ducts typically involves the application of different operating principles of sound attenuation: Dissipative through friction in fibrous and porous materials or in submillimeter slots and pores, reactive by reflection or by interference at, for example, $\lambda/4$-resonances [1–4]. These two principles can also occur together when the effect of the spring-mass oscillator is combined with the $\lambda/4$-resonance in a Helmholtz resonator. As an alternative to the methods described above, so-called Herschel-Quincke liners can be used, which are characterized by destructive interference via an U-shaped bypass [4].

Dissipative sound absorbers in HVAC and ventilation systems or automotive sound absorbers often use fibrous materials due to their effectiveness and cost-effectiveness. However, a disadvantage of these materials is that the acoustic effect can diminish if they become contaminated or damp. A lack of mechanical stability can also lead to dents in the sound attenuation, for example due to slippage of the material. Furthermore, flow can cause fibers to dissolve which can lead to health hazards, especially in HVAC systems [5–7]. An alternative proposed by Maa [8–10] in 1975 is the use of microperforated panels (MPP). MPPs are commercially available and typically made of plastic or metal and the cost is comparable to that of conventional porous or fibrous materials [11, 12]. Moreover, metallic MPPs are fire resistant and can be welded [11]. Furthermore, MPPs exhibit a flow-guiding effect with low pressure drop serving as sound-absorbing liners and baffles or as diffusors [6, 13]. The submillimeter openings in MPPs are usually circular or slot shaped. An alternative to panels with a large number of symmetrically arranged pores is the use of single slots extending over the entire cavity as back volume [14, 15].

MPPs are often paired with an air-filled cavity to create microperforated absorbers (MPA). These MPAs are characterized by frequency-specific damping maxima at the Helmholtz and/or $\lambda/4$-resonance. Using a single MPP results in narrowband damping maxima at the respective resonant frequencies, giving the silencer one degree of freedom. Alternatively, variants with several degrees of freedom can be used, resulting in more broadband attenuation [4]. For this purpose, the cavity is subdivided in depth direction with several perforated layers. Hence, these variants are also referred to as multi-layer MPAs [16]. Multi-layer MPAs can consist not only of MPPs, but additionally of fibrous or

*Corresponding author: benedikt.berchtenbreiter@fau.de

porous absorbers such as rock wool. The use of porous layers also leads to a more broadband attenuation and, additionally, to a shift of the resonant frequencies towards lower frequencies with the same total back volume [2, 17, 18].

A literature review focusing on the fabrication and materials used with respect to multi-layer MPAs with and without porous absorbers reveals that MPPs are typically fabricated from metallic materials [4, 19–22]. However, the production of MPPs also employs additive manufacturing with plastics [16, 23–25]. A wide variety of materials is used as porous absorbers: Glass and rock wool [17, 18, 26], vegetable fibers [16, 23, 27], foams [20, 22, 23], organic materials [28]. The authors of this paper are not aware of any studies in which the porous absorbers are additively manufactured.

Regarding additively manufactured porous absorbers, three structural types are typically distinguished in the literature: tubes [24, 29–31], lattice structures [32–42], cell structures [25, 43, 44]. In much of the research, the absorbers are built as lattice structures and are typically fabricated using fused deposition modelling (FDM). The advantage of the FDM process is that it is cost-effective, there is no need to remove excess polymer or powder after the printing process, and the fineness of the lattices is limited only by the diameter of the extrusion nozzle. Therefore, it is possible to produce very fine and close-meshed lattice structures. In addition, very high and low porosities can be realized with only one process. At this point, it is not possible to state which approach mentioned in the various papers yields the best results for sound dissipation, as the absorbers investigated differ in depth and, consequently, in effective volume. According to Cai et al. [33], however, the absorption becomes maximum when half the pore size or half the distance between adjacent lattice bars corresponds to the viscous boundary layer thickness.

When designing multi-layer MPAs, additively manufactured porous absorbers as acoustic metamaterial offer the advantage of specifically tailoring and adapting the acoustic properties to meet desired impedance boundary conditions. This opens up additional degrees of freedom in the design of multi-layer MPAs and is thus a decisive advantage of additively manufactured porous absorbers. Furthermore, the dimensional stability in combination with the geometric freedoms enables manufacturing according to the subsequent installation situation, for example when a multi-layer MPA is installed in a channel bend.

The objective of the present work was to design and validate double-layer MPA acoustic liners using additively manufactured porous absorbers. These liners combine a MPP, an additively manufactured porous absorber and a cavity and are tuned to a target frequency at which the damping maximum occurs. The absorber is positioned directly below the MPP inside the cavity so as not to lose the MPP's flow guiding. The back volume was divided both longitudinally and transversely, allowing for the assumption of a locally reacting liner in the modelling. The porous absorber was designed as a lattice structure due to its lower complexity compared to the cellular structure. Typically, lattice-type absorbers are manufactured using FDM. However, the FDM process is slow, limiting its applicability for large-scale industrial production. In the context of this work, the use in an industrial environment should already be considered. Therefore, the lattices were produced by means of binder jetting. With modern material systems, the process is characterized by a high level of detail, fast production times and low costs.

The focus of this work was to investigate the use and the advantages of additively manufactured porous absorbers. Therefore, the MPPs were fabricated by laser cutting and not additively, as this would have led to additional challenges and uncertainties, especially in the modelling of the impedance. To reduce the complexity of the MPPs, they were slotted, with each cavity being assigned one slot extending along its entire length. The primary question in this work was whether the acoustic effect of the additively manufactured absorbers is sufficient to achieve the described advantage of reducing the total back volume. Furthermore, for the design of the liners, it was necessary to succeed in modelling the acoustic properties of the porous absorbers as a function of geometry.

2 Acoustic modelling of MPAs

When a plane wave hits both a MPA or a multi-layer MPA perpendicularly according to Figure 1, the acoustic modelling is based on the surface impedance. The surface impedance $\underline{Z}_{\mathrm{MPA}}$ of a conventional MPA with one MPP and an air-filled cavity is determined as follows:

$$\underline{Z}_{\mathrm{MPA}} = \underline{Z}_{\mathrm{MPP}} - jZ_0 \cot\left(k_0 t_{\mathrm{C}}\right). \tag{1}$$

In equation (1), $\underline{Z}_{\mathrm{MPP}}$ denotes the impedance of the MPP, while Z_0 is the characterisic impedance of air. The free-field wavenumber is k_0 and the depth of the cavity is t_{C}.

2.1 Acoustic modelling of double-layer MPAs

The impedance of a multi-layer MPA with n layers in general is computed using equation (2), which is derived from the total transfer matrix $\mathbf{T}_{\mathrm{tot}}$ of the individual layers. $\mathbf{T}_{\mathrm{tot}}$ is obtained by multiplying the transfer matrices of each layer. For a double-layer MPA this denots multiplying $\mathbf{T}_{\mathrm{MPP}}$ of the MPP, $\mathbf{T}_{\mathrm{A}}$ of the porous absorber and $\mathbf{T}_{\mathrm{C}}$ of the air-filled cavity. [16, 19, 45, 46]

$$\underline{Z}_{\mathrm{DL}} = \frac{T_{\mathrm{tot},11}}{T_{\mathrm{tot},21}} \quad \text{with} \quad \mathbf{T}_{\mathrm{tot}} = \begin{bmatrix} T_{\mathrm{tot},11} & T_{\mathrm{tot},21} \\ T_{\mathrm{tot},21} & T_{\mathrm{tot},22} \end{bmatrix}$$

$$= \prod_{i=1}^{n} \left(\mathbf{T}_i\right) = \mathbf{T}_{\mathrm{MPP}} \cdot \mathbf{T}_{\mathrm{A}} \cdot \mathbf{T}_{\mathrm{C}}. \tag{2}$$

In equation (2), the transfer matrices of the layers are

$$\mathbf{T}_{\mathrm{MPP}} = \begin{bmatrix} 1 & \underline{Z}_{\mathrm{MPP}} \\ 0 & 1 \end{bmatrix}, \mathbf{T}_{\mathrm{A}} = \begin{bmatrix} \cos\left(\tilde{k}_{\mathrm{A}} t_{\mathrm{A}}\right) & j\tilde{Z}_{\mathrm{A}} \sin\left(\tilde{k}_{\mathrm{A}} t_{\mathrm{A}}\right) \\ j\frac{1}{\tilde{Z}_{\mathrm{A}}} \sin\left(\tilde{k}_{\mathrm{A}} t_{\mathrm{A}}\right) & \cos\left(\tilde{k}_{\mathrm{A}} t_{\mathrm{A}}\right) \end{bmatrix},$$

$$\mathbf{T}_{\mathrm{C}} = \begin{bmatrix} \cos\left(k_0 t_{\mathrm{C}}\right) & jZ_0 \sin\left(k_0 t_{\mathrm{C}}\right) \\ j\frac{1}{Z_0} \sin\left(k_0 t_{\mathrm{C}}\right) & \cos\left(k_0 t_{\mathrm{C}}\right) \end{bmatrix}. \tag{3}$$

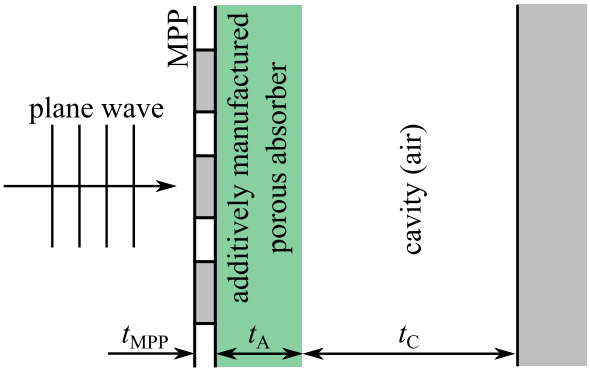

Figure 1. Schematic illustration of a double-layer MPA at perpendicular sound incidence.

In equation (3), the propagation of sound within the porous absorber is characterized by the complex equivalent wavenumber $\tilde{k}_{\mathrm{A}}$ and impedance $\tilde{Z}_{\mathrm{A}}$. The parameter t is used to describe the depth of the respective layer. Equation (2) simplifies to equation (1) for a conventional MPA with MPP and cavity.

2.2 Modelling of slotted MPPs

In this work, the modelling of the slotted MPPs is done using the Johnson, Champoux and Allard (JCA) semiphenomenological model [46–48] according to equation (4). Here ρ_0 is the density and υ is the kinematic viscosity of air and ϕ_{MPP} is the degree of perforation of the MPP. The viscous characteristic length Λ corresponds to the hydraulic radius r_{hyd} of the slots. The static flow resistance with $\sigma = 12\upsilon\rho_0/r_{\mathrm{hyd}}$ is also calculated as a function of the hydraulic radius. The tortuosity $\alpha_\infty = 1 + 2\epsilon/t_{\mathrm{MPP}}$ is a function of both the correction length ϵ and the depth of the MPP.

$$\underline{Z}_{\mathrm{MPP}} = j\omega t_{\mathrm{MPP}} \frac{\rho_0}{\phi_{\mathrm{MPP}}} \left\{ \alpha_\infty + \frac{\sigma\phi_{\mathrm{MPP}}}{j\omega\rho_0} \left[1 + \left(\frac{2\alpha_\infty\rho_0}{\phi_{\mathrm{MPP}}\Lambda\sigma} \right)^2 \frac{j\omega}{\upsilon} \right]^{\frac{1}{2}} \right\}. \tag{4}$$

In the literature, different approaches are considered to calculate the correction length ϵ. Attala and Sgard [49] propose $\epsilon = 0.85 r_{\mathrm{hyd}}$. Zieliński et al. [50] choose the following approach for parallel slots using the slot width w_{S} and the distance w_0 of adjacent slots:

$$\epsilon = \frac{\xi w_0}{\pi} \sum_{m=1}^{\infty} \frac{1}{m} \left[\frac{\sin(m\pi\xi)}{m\pi\xi} \right]^2 \text{with} \quad \xi = \frac{w_{\mathrm{S}}}{w_0}. \tag{5}$$

Investigations in [51] have shown that for the geometrical characteristics of the perforated panels of this work, the approach by Attala and Sgard [49] is advantageous for slot widths in the range of 0.4 mm, while the approach by Zieliński et al. [50] is preferable for slot widths larger than 1 mm. The range in between thus represents a transition. When designing the liners in Section 4, it should be possible to model the impedance of the MPP as a continuous function of the slot width. Therefore, a resulting correction length that accounts for the transition region was formed from both approaches. The course of the correction length over the slot width is shown in Figure 2.

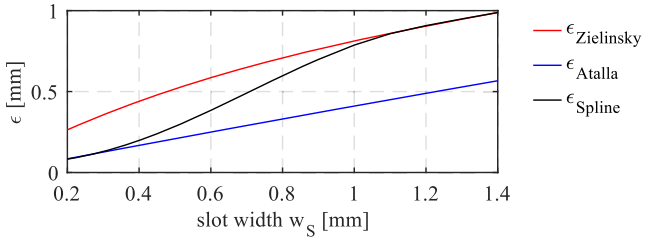

Figure 2. Correction lengths ϵ according to Zieliński et al. [50] and Attala and Sgard [49] as well as the spline fitted from them as a continuous function of w_{S}.

The influence of the porous absorber underneath the MPP on the fluid motion in the orifices was considered using the dynamic approach proposed in [49]. With an additional reactance term, the dynamic approach takes into account the resistive and inertial effects due to the distortion of the fluid movement in the porous absorber at the interface to the MPP.

2.3 Modelling of additively manufactured porous absorbers

In the model, additively manufactured porous absorbers are treated as an equivalent fluid and the sound propagation in the fluid is characterized by complex quantities, namely equivalent density $\tilde{\rho}$ and equivalent bulk modulus $\tilde{K}$. The modelling of $\tilde{\rho}$ and $\tilde{K}$ of the additively manufactured porous absorbers was performed using the Johnson, Champoux, Allard, and Lafarge (JCAL) semi phenomenological model [47, 48, 52, 53] corresponding to the equations (6) and (7) [46]:

$$\tilde{\rho}(\omega) = \frac{\rho_0}{\phi} \left[\alpha_\infty + \frac{\upsilon\phi}{j\omega q_0} \tilde{G}(\omega) \right] \quad \text{with}$$

$$\tilde{G}(\omega) = \left[1 + \left(\frac{2\alpha_\infty q_0}{\phi\Lambda} \right)^2 \frac{j\omega}{\upsilon} \right]^{\frac{1}{2}}, \tag{6}$$

$$\tilde{K}(\omega) \frac{\gamma p_0}{\phi} \left[\gamma - \frac{\gamma - 1}{1 + \frac{\upsilon'\phi}{j\omega q_0'} \tilde{G}'(\omega)} \right]^{-1} \quad \text{with}$$

$$\tilde{G}' = \left[1 + \left(\frac{2q_0'}{\phi\Lambda} \right)^2 \frac{j\omega}{\upsilon'} \right]^{\frac{1}{2}}. \tag{7}$$

The equivalent density $\tilde{\rho}$ and the equivalent bulk modulus $\tilde{K}$ depend on the following fluid properties of air: density ρ_0, kinematic viscosity υ, isentropic exponent γ, Prandtl number Pr with $\upsilon' = \upsilon/Pr$. In addition, the modelling is based on the so-called JCAL parameters resulting from the micro geometry of the porous absorber: Porosity ϕ, tortuosity α_∞, viscous characteristic length Λ, thermal characteristic length Λ', static viscous permeability q_0 static thermal

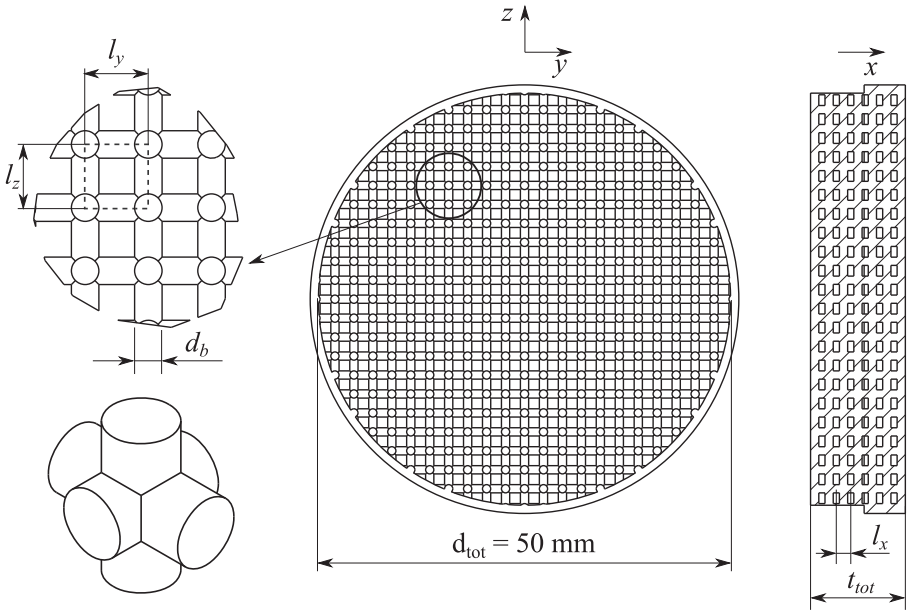

Figure 3. Geometric structure of the investigated additively manufactured porous absorbers including the elementary cell (bottom left).

permeability q_0'. While the fluid properties of air can be measured and calculated directly, the corresponding JCAL parameters are determined using an inverse scheme (see Sect. 3.1).

3 Experimental characterization of additively manufactured porous absorbers

The additively manufactured porous absorbers represent a periodically arranged lattice structure according to Figure 3 and were manufactured from polymethyl acrylate by means of binder jetting. According to Table 1, the lattice constant l_{yz} in yz-direction was systematically varied. This led to lattice structures with different porosities ϕ_{CAD}, which were determined using the CAD (Computer Aided Design) data. The diameter of the bars d_b is 0.5 mm.

The acoustic properties of the porous absorbers were determined in the two-port test rig TPP-K (Two-Port-Prüfstand Kreisförmiger Querschnitt) [51] at FAU Erlangen-Nuremberg. Transmission, reflection and dissipation were determined as well as the equivalent fluid properties $\tilde{\rho}(\omega)$ and $\tilde{K}(\omega)$ via the transfer matrix method. The procedure and results are described in detail in [51].

3.1 Characterization of the JCAL parameters via inverse scheme

In order to model the additively manufactured porous absorbers as a continuous function of the lattice constant, the initial step involved determining the JCAL parameters x_{JCAL} for each absorber in Table 1. One sample was manufactured for each absorber and its equivalent density $\tilde{\rho}$ and equivalent bulk modulus $\tilde{K}$ were determined using the measured transfer matrix. Based on a constrained minimization problem, an inverse scheme was employed to determine the JCAL parameters. The discrepancy between the modeled and experimentally determined values for $\tilde{\rho}$ and $\tilde{K}$ forms the cost function, to be iteratively minimized. In this way, it is possible to fit the JCAL parameters of the model to the real parameters of the absorbers. Using the Euclidean norm $\|\bullet\|$, the cost function to be minimized g_{min} is as follows [54]:

$$g_{min}(\omega, x_{JCAL}) = W_{\tilde{\rho}} \|\tilde{\rho}_{exp}(\omega) - \tilde{\rho}_{JCAL}(\omega, \phi, \alpha_\infty, \Lambda, q_0)\|^2 + W_{\tilde{K}} \|\tilde{K}_{exp}(\omega) - \tilde{K}_{JCAL}(\omega, \phi, \Lambda', q_0')\|^2 . \quad (8)$$

The weighting factors $W_{\tilde{\rho}}$ and $W_{\tilde{K}}$ are computed using the length N of the frequency vector:

$$W_{\tilde{\rho}} = \frac{1}{\rho_{RMS}^2} \quad \text{with} \quad \rho_{RMS} = \frac{\|\tilde{\rho}_{exp}\|}{\sqrt{N}} \quad \text{and}$$
$$W_{\tilde{K}} = \frac{1}{K_{RMS}^2} \quad \text{with} \quad K_{RMS} = \frac{\|\tilde{K}_{exp}\|}{\sqrt{N}} . \quad (9)$$

The solution of the minimization problem is thus

$$\hat{x}_{JCAL} = \arg\min_{x_{JCAL}} g_{min}(\omega, x_{JCAL}) . \quad (10)$$

Table 1. Characteristic geometric parameters of the additively manufactured porous absorbers.

d_b [mm]	l_x [mm]	l_{yz} [mm]	ϕ_{CAD} [%]	t_t [mm]
0.5	1.25	1.25	71	10.5
0.5	1.25	1.36	74	10.5
0.5	1.25	1.52	77	10.5
0.5	1.25	1.65	79	10.5
0.5	1.25	2.00	83	10.5

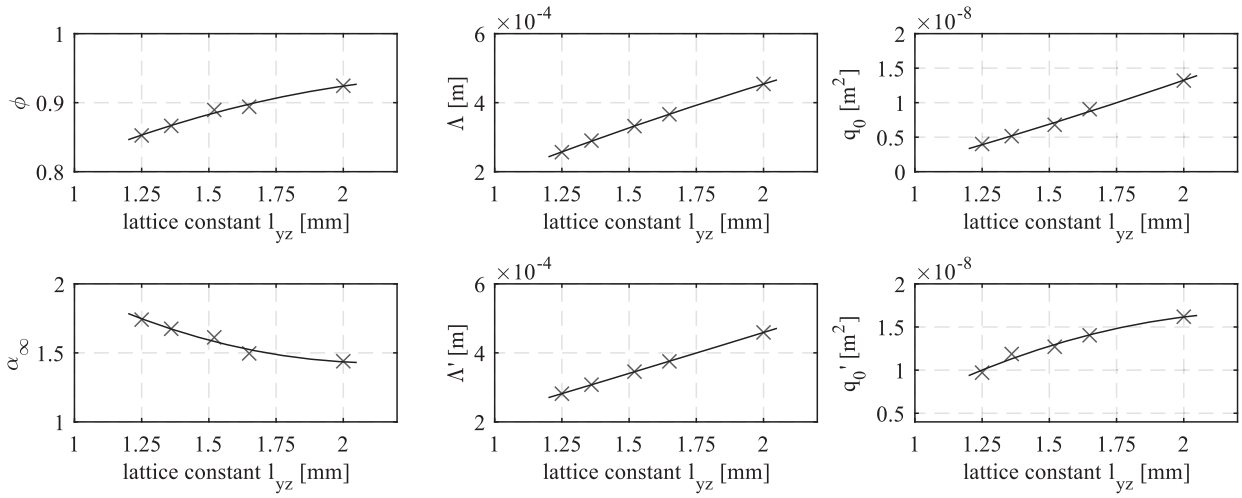

Figure 4. Mean values of the inverse determined JCAL parameters for each lattice constant l_{yz} (×) and the fitted functions based on it.

The minimization was solved using an interior-point algorithm adhering to the constraints proposed by Niskanen et al. [54]: $0 \leq \phi \leq 1, \leq \alpha_\infty \leq 10, 10 \cdot 10^{-6} \leq \Lambda, \Lambda' \leq 2000{\cdot}10^{-6}$ m, $0.1 \cdot 10^{-9} \leq q_0, q_0' \leq 100 \cdot 10^{-9}\,\mathrm{m}^2$, $\Lambda_0' \geq \Lambda_0, q_0' \geq q_0$. To increase the probability of finding a solution for each lattice structure that is as close as possible to the global minimum and thus to the putative optimal parameters, the minimization was solved 10,000 times. The initial values were chosen randomly within the above limits. Subsequent the parameters associated with the lowest function values of the 10,000 minima of $g_{\min}$ were examined. It was observed that there are differences between the parameters, despite the associated function values being remarkably similar. This means that there is a set of parameter combinations with which $\tilde{\rho}$ and $\tilde{K}$ can be modeled in a very good approximation. As a result, the parameter combinations of the 50 lowest function values were selected and the mean value for each parameter was calculated, rather than selecting the parameters associated with the global of the 10,000 minima. With this approach, the best results were obtained in the validation of the inverse scheme.

Finally, by fitting, the individual parameters were determined as a continuous function of the lattice constant l_{yz}. It should be pointed out that when fitting the functions, the main focus was to be able to model the equivalent fluid properties between $l_{yz,\min}$ and $l_{yz,\max}$ as accurately as possible. Therefore, the functions should not be extrapolated. The best fitting results were obtained with a quadratic polynomial curve. Figure 4 shows the JCAL parameters as a function of the lattice constant.

As expected, the porosity ϕ decreases with decreasing lattice constant, thereby increasing filling ratio. Upon comparing the values with the design data for each lattice constant, it becomes evident that the values inversely determined surpass those computed using CAD data. Therefore, the structures were viewed under a microscope and the dimensions of the lattice bars were measured. Assuming rotational symmetry of the lattice bars, the diameters were measured at several positions and an average diameter of 0.48 mm was calculated. This reduction in diameter would correspond to a reduction in the volume of the lattice structure by 8.2%, thereby an increase in porosity. This consideration is a very idealized and simplified calculation, which is intended to illustrate the enormous influence geometric deviations have on the porosity. This serves as an explanatory approach for the discrepancy observed between theoretical and inversely determined porosity.

The tortuosity decreases with increasing lattice constant and porosity. This characteristic aligns with the results obtained by Boulvert et al. [38] in similar studies. In the range considered, both the viscous and thermal characteristic lengths Λ and Λ' increase approximately linearly with the lattice constant l_{yz}. This is consistent with expectations given that the lattice constant represents the characteristic geometric dimension of the lattice structures. The characteristic lengths of the different lattice constants are of the order of half the length of the free space of adjacent lattice bars. The curves for the viscous and thermal characteristic length are almost identical. This can be attributed to the fact that the lattice structures are not pores in the classical sense with constrictions and expansions. This results in the characteristic lengths being attributed to the same geometric dimension. This result is also confirmed by Boulvert et al. [38]. Thus, the determined characteristic lengths are plausible both qualitatively and quantitatively.

Finally, the static viscous and thermal permeabilities q_0 and q_0' are considered. Both parameters increase with the lattice constant and porosity, as expected. Once again, this behavior aligns with the research of Boulvert et al. [38]. The values obtained are also quantitatively similar to their results. The static viscous permeability is directly related to the flow resistance σ of the lattice structures as expressed by the equation $\sigma = \nu\rho_0/q_0$, and it decreases with increasing permeability. A decreasing flow resistance with increasing lattice constant corresponds to the fluid mechanical expectations. In conclusion, the static permeabilities, both quantitatively and qualitatively, appear to be plausible.

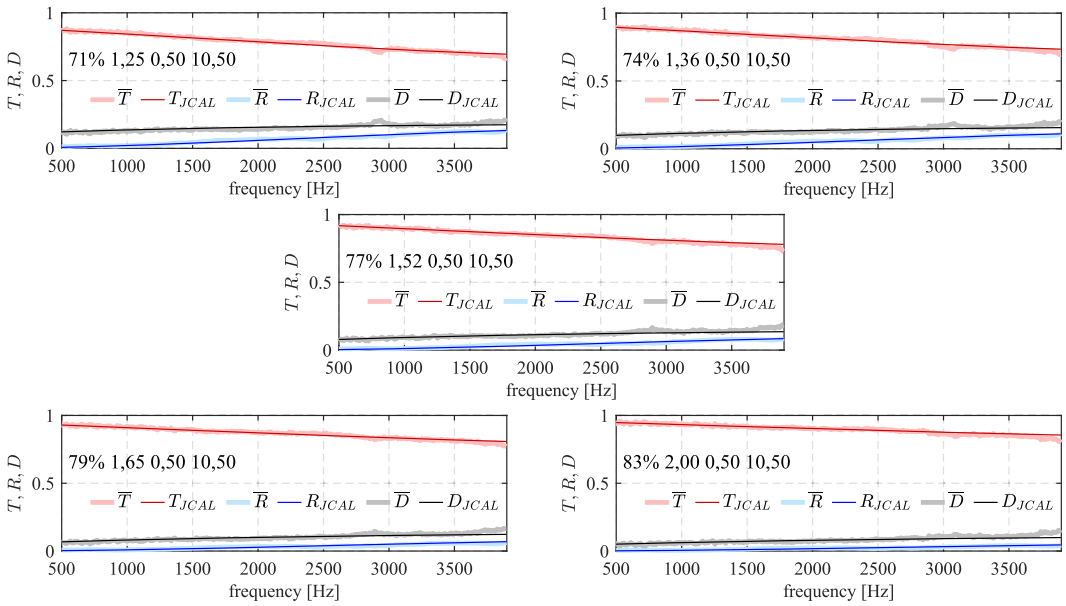

Figure 5. Transmission, reflection, and dissipation: measured data ($\overline{T}$, $\overline{R}$, $\overline{D}$) and modeled data (T_{JCAL}, R_{JCAL}, D_{JCAL}).

3.2 Validation of the inverse scheme

The final step in the inverse scheme is its validation. To achieve this, the reflection, dissipation and transmission are reconstructed using the function values of the JCAL parameters and these are then compared with the corresponding measurement values of each absorber listed Table 1. The steps in this process are listed below:

1. Determination of the JCAL parameters by reading the corresponding functions depending on the lattice constant l_{yz}.
2. Calculation of $\tilde{\rho}(\omega)$ and $\tilde{K}(\omega)$ with the JCAL model according to the equations (6) and (7).
3. Calculation of the equivalent wave number $\tilde{k}(\omega)=\omega\sqrt{\frac{\tilde{\rho}}{\tilde{K}}}$ and equivalent impedance $\tilde{Z}(\omega)=\sqrt{\tilde{\rho}\tilde{K}}$.
4. Calculation of the transfer matrix $\mathbf{T}(\omega)$ with equation (3).
5. Calculation of reflection and transmission as energy quantities $R(\omega)$ und $T(\omega)$ [55]:

$$R(\omega)=|\underline{\rho}(\omega)|^2=\left|\frac{2e^{j\tilde{k}t_{\mathrm{G}}}}{T_{11}+\frac{T_{12}}{Z_0}+Z_0T_{21}+T_{22}}\right|^2,$$

$$T(\omega)=|\underline{\tau}(\omega)|^2=\left|\frac{T_{11}+\frac{T_{12}}{Z_0}-Z_0T_{21}-T_{22}}{T_{11}+\frac{T_{12}}{Z_0}+Z_0T_{21}+T_{22}}\right|^2. \quad (11)$$

6. Calculation of the dissipation $D(\omega)=1-(R+T)$.

Figure 5 shows the modeled and measured curves for transmission, reflection and dissipation of the absorbers according to Table 1. Model and measurement agree very well in the considered frequency range. Upon considering the upper frequency range, it becomes apparent that for all configurations with the JCAL model the dissipation is slightly underestimated when compared to the measurements. This difference is due to the higher dissipation error when the frequency is close to the upper cut-off frequency of the TPP-K [51]. The significance of the dissipation error increases as the measured dissipation decreases. In contrast, this implies that modelling succeeds in eliminating or reducing the systematic dissipation error of the test rig at high frequencies. The same is true for dissipation due to structural vibrations, which depend only on the geometry of the overall lattice structure with d_{tot} and t_{tot} (see Fig. 3) and do not represent any acoustic property of the lattice as an equivalent fluid per se. For instance, in the measured data, an increased dissipation occurs at 2900 Hz for $l_{\mathrm{yz}}=1.25$ mm, attributed to a structural vibration of the overall structure, but this is not evident in the modeled curve. Thus, the inverse scheme's ability to reduce or eliminate the influence of measurement uncertainties and structural oscillations, which are dependent on the overall geometry of the measured absorbers, is a significant advantage. This enhancement increases the anticipated accuracy of the results when the equivalent fluid properties are utilized for subsequent calculations, such as numerical simulations or analytical models.

4 Design of double-layer MPA liners

The double-layer MPA liners (DLMPA) were designed according to Section 2 by modelling the surface impedance. This methodology is equally applicable for liners if the boundary condition of a locally reacting wall is fulfilled. Locally reacting implies that the acoustic behaviour does not depend on the spatial geometry of the sound field, and thus not depend on the angle of incidence. Figure 6 shows the structure of the liners based on CAD data. The entire liner consists of 36 double-layer MPAs. The absorber elements are positioned within the cavities and are directly

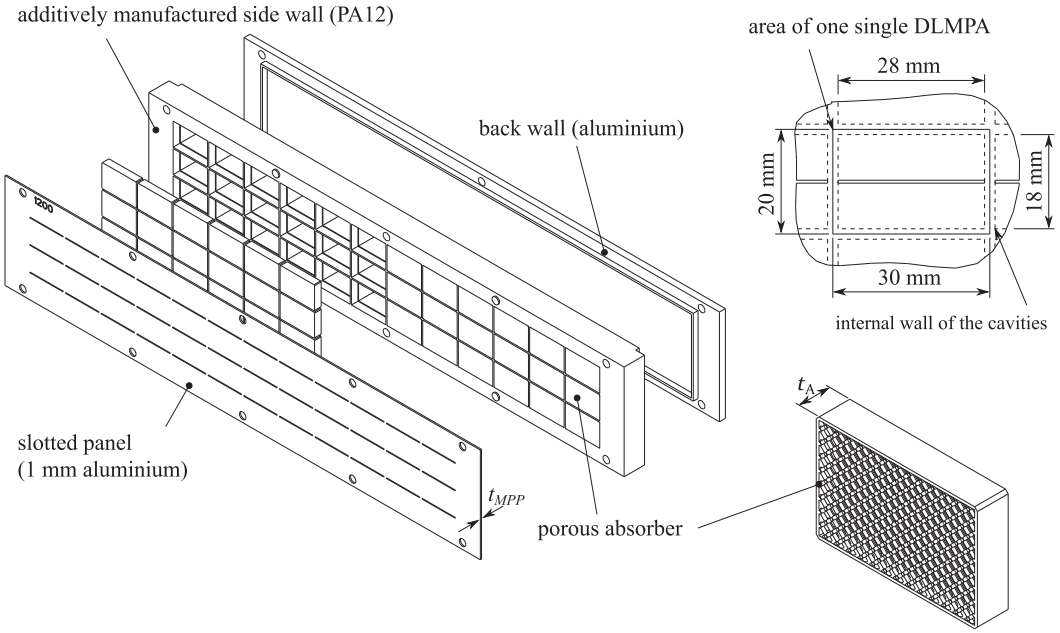

Figure 6. Liner consisting of 36 DLMPA: general view (left), detailed view (top right), porous absorber (bottom right).

connected to the MPP. The characteristic dimensions l_{char} of the cavities are 18 mm (width) and 28 mm (length). With resonant frequencies up to 1500 Hz, the boundary condition of a locally reacting liner with $k_0 l_{\mathrm{char}} \ll 1$ [56] is thus fulfilled. The wall thickness of the cavities is 2 mm. Thus, the acoustically effective length of the liners is 360 mm. The MPP was fabricated of 1 mm aluminum sheet by laser cutting. According to Figure 7, the liners are designed for the two-port test rig TPP-R (Two-Port-Prüfstand Rechteckiger Querschnitt) [51]. The cross-section of the flow-carrying channel is 60 mm × 80 mm.

The design of the liner targeted the optimum wall impedance according to Cremer [57], at which the maximum damping occurs. Taking into account the losses in the wall boundary layer, the optimal wall impedance of a single-sided liner in a rectangular duct is [56]

$$\frac{\underline{Z}_{\mathrm{opt}}}{\rho_0 c_0} = (0.929 - 0.7468j)\frac{2f_{\mathrm{opt}}h}{c_0}\,. \tag{12}$$

The distance to the opposite wall is h. Two liners were specifically designed with the target frequencies $f_{\mathrm{opt}} = 800$ Hz and 1200 Hz. The surface impedance of the liners $\underline{Z}_{\mathrm{W}}$ was calculated using the equations (2)–(7). The impedance was related to the entire channel width and the wall thickness of the cavities was considered (see Fig. 6):

$$\underline{Z}_{\mathrm{W}} = \frac{A_{\mathrm{Wand}}}{A_{\mathrm{DL}}}\underline{Z}_{\mathrm{DL}} = \frac{36\,(20\mathrm{mm}\cdot 30\mathrm{mm})}{36\,(18\mathrm{mm}\cdot 28\mathrm{mm})}\underline{Z}_{\mathrm{DL}} = \frac{1}{\phi_{\mathrm{DL}}}\underline{Z}_{\mathrm{DL}}\,. \tag{13}$$

Using a genetic algorithm, $\underline{Z}_{\mathrm{W}}$ was iteratively fitted to $\underline{Z}_{\mathrm{opt}}$ for the two target frequencies. Four geometric degrees of freedom x_{geo} were available: 0.4 mm $\leq w_{\mathrm{S}} \leq$ 1.2 mm, $0 \leq t_{\mathrm{C}}$, 1.25 mm $\leq l_{\mathrm{yz}} \leq$ 2.0 mm, 3.75 mm $\leq t_{\mathrm{A}} \leq$ 10 mm. Thus, the function to be minimized was

$$g_{\min}\left(x_{\mathrm{geo}}, f_{\mathrm{opt}}\right) = \left[(0.929 - 0.7468i)\frac{2f_{\mathrm{opt}}h}{c_0}\right] - \frac{\underline{Z}_{\mathrm{W}}\left(x_{\mathrm{geo}}\right)}{\rho_0 c_0}\,. \tag{14}$$

The minimization problem was solved 200 times with a randomly varying set of initial values using the Matlab function *ga* with the recommended default settings [58]. Table 2 gives the parameter combinations with the lowest function values for $g_{\min}$. Furthermore, it shows the deviations $\Delta_{\underline{Z},\Re}$ and $\Delta_{\underline{Z},\Im}$ from $\underline{Z}_{\mathrm{opt}}$ for the respective real and imaginary parts. The total depth is $t_{\mathrm{tot}} = t_{\mathrm{C}} + t_{\mathrm{A}}$.

For both target frequencies, $f_{\mathrm{opt}} = 800$ Hz and 1200Hz, the genetic algorithm succeeded in determining parameter sets which approximate $\underline{Z}_{\mathrm{opt}}$ quite accurately. It is evident that the optimal wall impedance is well approximated across different parameter sets. This therefore means that the optimum wall impedance is achieved with different parameter sets. When designing the liners, it is thus possible to choose from various options. For example, the variant that is most advantageous in terms of production can be selected.

To check if the required back volume is reduced with the additively manufactured porous absorbers beneath the MPP, corresponding variants without absorbers were designed for the two target frequencies. To distinguish clearly, these are referred to as single-layer MPA liners (SLMPA). The basic procedure was identical to the double-layer variants, with the distinction that only two degrees of freedom were available in the depth of the cavity and the slot width. The following result was achieved:

- Single-layer MPA with $f_{\mathrm{opt}} = 800$ Hz: $t_{\mathrm{C}} = t_{\mathrm{tot}} = 47.32$ mm and $w_S = 0.56$ mm.
- Single-layer MPA with $f_{\mathrm{opt}} = 1200$ Hz: $t_{\mathrm{C}} = t_{\mathrm{tot}} = 22.41$ mm and $w_S = 0.48$ mm.

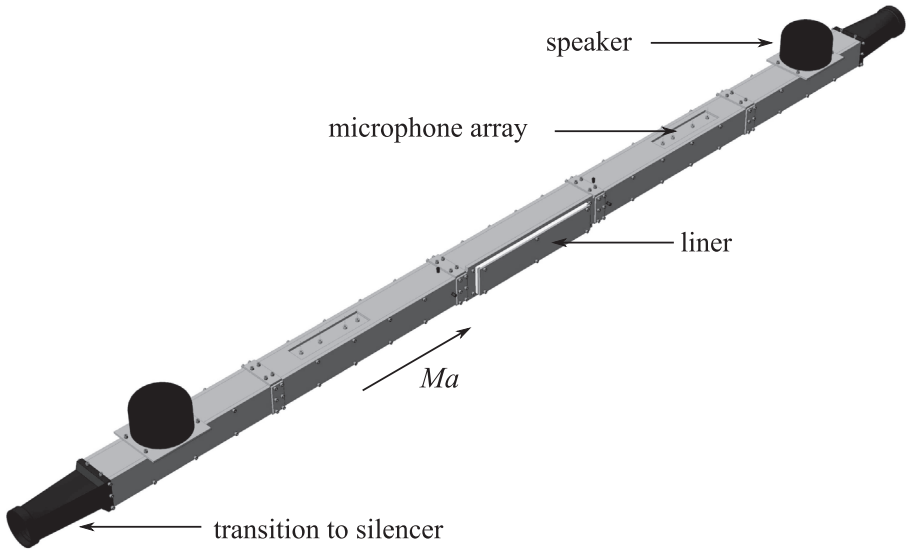

Figure 7. CAD model of the symmetrically designed TPP-R.

Table 2. Parameter sets with the lowest function values for $g_{\min}$.

f_{opt} [Hz]	t_{tot} [mm]	t_{C} [mm]	w_{S} [mm]	l_{yz} [mm]	t_{A} [mm]	$\Delta_{\underline{Z},\Re}$ [%]	$\Delta_{\underline{Z},\Im}$.[%]	Variant
800	41.68	33.09	0.73	1.53	8.59	$1.5 \cdot 10^{-4}$	$7.8 \cdot 10^{-5}$	1
800	42.33	36.73	0.66	1.62	5.60	$2.6 \cdot 10^{-5}$	$2.3 \cdot 10^{-4}$	2
800	42.22	38.21	0.64	1.53	3.99	$1.1 \cdot 10^{-4}$	$3.1 \cdot 10^{-4}$	3
800	41.65	37.16	0.67	1.41	4.49	$2.6 \cdot 10^{-4}$	$3.8 \cdot 10^{-4}$	4
800	41.00	36.79	0.71	1.25	4.21	$3.8 \cdot 10^{-4}$	$1.5 \cdot 10^{-4}$	5
1200	20.52	11.49	0.59	1.67	9.04	$8.7 \cdot 10^{-6}$	$1.9 \cdot 10^{-5}$	1
1200	20.20	14.66	0.56	1.51	5.54	$1.4 \cdot 10^{-4}$	$3.6 \cdot 10^{-4}$	2
1200	20.71	10.78	0.59	1.82	9.93	$3.7 \cdot 10^{-4}$	$1.9 \cdot 10^{-4}$	3
1200	19.97	10.51	0.68	1.30	9.46	$4.2 \cdot 10^{-4}$	$2.8 \cdot 10^{-5}$	4
1200	20.26	10.96	0.62	1.48	9.30	$4.1 \cdot 10^{-4}$	$1.4 \cdot 10^{-4}$	5

For the single-layer MPAs, $\underline{Z}_{\text{opt}}$ is obtained with only one parameter set. Table 3 compares the total depths of the different parameter sets of the double-layer MPAs with the total depth of the single-layer MPAs. It has been confirmed that the additively manufactured porous absorbers significantly reduce the necessary total back volume by up to 13.4%.

5 Experimental validation

The two-port test rig TPP-R [51] was utilized for experimental validation. For each of the two target frequencies, one double-layer MPA and one single-layer MPA liner was manufactured. Due to manufacturing considerations, variant 2 (see Tab. 2) was selected for the double-layer MPAs in each case. Variant 2 combines two advantages for both target frequencies. Firstly, the lattice constant is moderate and not too fine-meshed. This allows the excess powder to be removed after additive manufacturing without high energy input. This reduces the risk of destroying the fine lattice bars and the production time. Secondly, with a total depth of 5.6 mm and 5.4 mm respectively, it was possible to design the lattice structures in such a way that the bars end with their full diameter. This prevented the bars in the edge layers from becoming too thin and being damaged when the excess powder was removed. Figure 8 shows the measured transmission loss as a function of frequency. The measurements were conducted without channel flow. A distinction is made between the total transmission loss TL, that due to dissipation TL_{D} and that due to reflection TL_{R}.

Table 4 presents a comparison between the frequencies $f_{\text{D}_{\max}}$, where the damping maxima occur, and f_{opt} according to the design in the previous section. For all four liners there is a very good agreement with a maximum of 2.8% deviation between measurement and design.

For the DL800 and SL800, f_{opt} is marginally overestimated, while for the DL1200 and SL1200, it is underestimated. Consequently, there is not a clear dependency whether the modelling approach fundamentally under- or overestimates f_{opt}. However, it is evident that the agreement is better for $f_{\text{opt}} = 800$ Hz than for 1200 Hz. One possible reason for this may be that the impedance models for low frequencies are more resilient to geometric deviations due to tolerances in manufacturing. An alternative cause

Table 3. Differences in total depth of the DLMPAs and SLMPAs for f_{opt} = 800 Hz and 1200 Hz.

f_{opt} [Hz]	$t_{tot.SLMPA}$ [mm]	$t_{tot.DLMPA}$ [mm]	Reduction [%]	f_{opt} [Hz]	$t_{tot.SLMPA}$ [mm]	$t_{tot.DLMPA}$ [mm]	Reduction [%]
800	47.32	41.68	11.9	1200	22.40	20.52	8.4
800	47.32	42.33	10.5	1200	22.40	20.20	9.8
800	47.32	42.20	10.8	1200	22.40	20.71	7.6
800	47.32	41.65	12.0	1200	22.40	19.97	10.9
800	47.32	41.00	13.4	1200	22.40	20.26	9.5

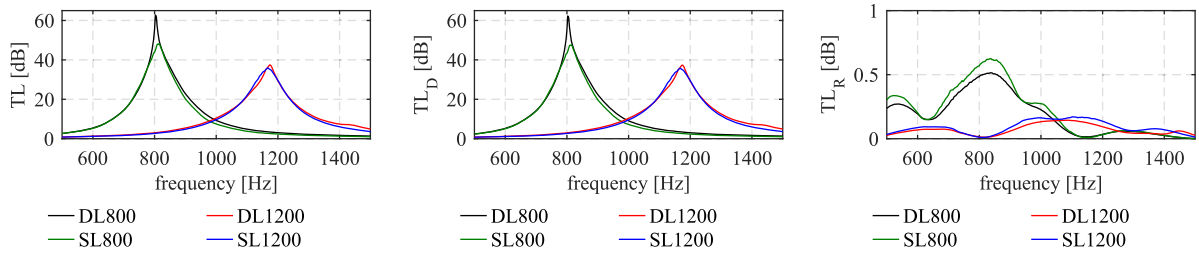

Figure 8. Transmission loss: total TL (left), by dissipation TL_D (middle), by reflection TL_R (right).

Table 4. Comparison of f_{opt} (design) and $f_{D_{max}}$ (measurement) for DL800, DL1200, SL800 and SL1200.

	f_{opt} [Hz]	$f_{D_{max}}$ [Hz]	Δf [%]
DL800	800	803	+0.4
SL800	800	812	+1.5
DL1200	1200	1175	−2.1
SL1200	1200	1166	−2.8

is inaccuracies in the modelling of the impedance. Since the characteristics of the DL1200 and SL1200, with and without absorber elements, are qualitatively very similar, this is an indication that the model for the impedance of the slotted MPP is less accurate with increasing frequency.

Figure 8 illustrates the transmission loss due to dissipation dissipation $\overline{TL}_D$ and reflection $\overline{TL}_R$. $\overline{TL}_D$ indicates that dissipation plays a significant role in the sound-absorbing effect of the liners. For all liners considered, $\overline{TL}_R$ is significantly below 1. This behavior corresponds to the characteristics of a liner with optimal wall impedance and confirms the modelling approaches with and without porous absorber.

According to the literature [2], an additional advantage of multi-layer MPAs is the more broadband damping characteristic. This feature does not occur with the liners investigated here. The transmission loss for frequencies larger and smaller than $f_{D_{max}}$ is similar. The dissipative effect of the porous absorbers is too small to have a noticeable effect due to the relatively large lattice constants. Therefore, future investigations should focus on producing and integrating additively manufactured porous absorbers with even lower lattice constants to increase dissipation. In this context, it is important to consider additive manufacturing processes that make it possible to reproducibly create very fine and close-meshed lattice structures, such as FDM.

6 Conclusion

The objective of this work was the design of double-layer MPA liners, which are a combination of MPP, additively manufactured porous absorber and cavity, and can be adapted to a target frequency where the maximum damping is expected to occur. For this purpose, it was essential to model the acoustic behavior of the porous absorbers as a function of the lattice constant. Consequently, the equivalent fluid properties were modeled using the JCAL model, based on experimental data. Continuous functions were fitted over the lattice constant for each JCAL parameter. The Validation of the JCAL model demonstrated a strong correlation between measurement and model in terms of transmission, reflection and dissipation of the absorbers studied.

The design of the double-layer MPA liners targeted the optimum wall impedance, according to Cremer [57]. Using a genetic algorithm, the impedance of the liners was iteratively adjusted to the optimum wall impedance. The degrees of freedom available in the design were the slot width of the MPP, the lattice constant and the depth of the absorber and of the air-filled cavity. It was determined that different parameter sets closely approximate the optimum impedance boundary condition. This is particularly advantageous, since the parameter set can be selected to fit to the requirement of the production technology. Alongside to the double-layer MPAs, comparable variants without porous absorber were designed. It was found that the required total back volume can be reduced by up to 13.4% by using the porous absorber. Finally, the liners underwent experimental validation. For both the single- and double-layer MPA liners, the target frequencies are met to a very good approximation. In addition, the transmission loss is primarily result of dissipation. This corresponds to the expectations for liners with optimal impedance boundary condition according to Cremer [57].

Contrary to what is described in the literature, a more broadband damping was not achieved with the double-layer MPAs compared to the single-layer MPAs.

Thus, the primary questions of this work can be answered. The additively manufactured porous absorbers can be effectively modeled as a function of geometry and this model has been successfully validated. The acoustic effect of the absorbers is substantial enough to achieve a reduction in the necessary back volume.

Based on the results of this work, future research should aim to enhance the complexity of double-layer MPAs by using MPPs with multiple circular or slot-shaped micro perforations. Additionally, it would be intriguing to observe the behaviour of double-layer MPAs when the absorber elements are positioned above the MPP, as well as the impact of the position of the absorber elements within the cavity on sound damping.

Conflicts of interest

The authors declared no conflicts of interests.

Data availability statement

Data are available on request from the authors.

References

1. M.L. Munjal: Acoustics of ducts and mufflers, 2nd edn., John Wiley & Sons Ltd, Chichester, 2014.
2. H.V. Fuchs: Schallabsorber und Schalldämpfer, 2nd edn., Springer-Verlag Berlin Heidelberg, Berlin Heidelberg, 2006.
3. M.J.T. Smith: Aircraft noise, Cambridge University Press, Cambridge, 1989.
4. S. Busse-Gerstengarbe: Untersuchung von lokal und nichtlokal reagierenden akustischen Dämpfern (Linern) für Triebwerke, PhD thesis, Technische Universität Berlin, 2015.
5. M. Villau, H. Rämmal, J. Lavrentjev: Innovative fibreless HVAC duct silencer based on microperforated elements, Materials Today: Proceedings 47 (2021) 3154–3160.
6. S. Allam, M. Åbom: Fan noise control using microperforated splitter silencers, Journal of Vibration and Acoustics 136 (2014) 031017-1–031017-8.
7. R. Kabral, L. Du, M. Åbom, M. Knutsson: A compact silencer for the control of compressor noise, SAE International of Engines 7, 3 (2014) 1574–1578.
8. D.-Y. Maa: Theory and design of microperforated panel sound-absorbing constructions, Scientia Sinica 18, 1 (1975) 55–71.
9. D. Maa: Microperforated-panel wideband absorbers, Noise Control engineering Journal 29, 3 (1987) 77–84.
10. D. Maa: Potential of microperforated panel absorber, The Journal of the Acoustical Society of America 105, 5 (1998) 2861–2866.
11. S. Floss, F. Czwielong, M. Kaltenbacher, S. Becker: Design of an in-duct micro perforated panel absorber for axial fan noise attenuation, Acta Acustica 5 (2021) 24.
12. S. Allam, M. Åbom: A new type of muffler based on microperforated tubes, Journal of Vibration and Acoustics 133, 3 (2011) 031005-1–031005-8.
13. M. Åbom, S. Allam: Dissipative silencers based on microperforated plates, in: Proceedings of 11th International Conference on Engines & Vehicles, Capri, Napoli, Italy, September 15–19, 2013.
14. P. Cobo, C. de la Colina, F. Simón: On the modelling of microslit panel absorbers, Applied Acoustics 159 (2020) 107118.
15. H. Zhao, Y. Wang, J. Wen, Y.W. Lam, O. Umnova: A slim subwavelength absorber based on coupled microslits, Applied Acoustics 142 (2018) 11–17.
16. Z. Liu, J. Zhan, M. Fard, L.J. Davy: Acoustic properties of multilayer sound with a 3D printed mirco-perforated panel, Applied Acoustics 121 (2017) 25–32.
17. F.-C. Lee, W.-H. Chen: Acoustic transmission analysis of multi-layer absorbers, Journal of Sound and Vibration 248, 4 (2001) 621–634.
18. W.A. Davern: Perforated facings backed with porous materials as sound absorbers – an experimental study, Applied Acoustics 10 (1977) 85–112.
19. D.H. Lee, Y.P. Kwon: Estimation of the absorption performance of multiple layer perforated panel systems by transfer matrix method, Journal of Sound and Vibration 278 (2004) 847–860.
20. R. Tayong, T. Dupont, P. Leclaire: Sound absorption of a micro-perforated plate backed by a porous material under high sound excitation: measurement and prediction, International Journal of Engineering & Technology 2, 4 (2013) 281.
21. J. Ning, Q. Geng, M.P. Arunkumar, Y. Li: Wide absorption bandwidth of a light composite absorber based on micro-perforated sandwich panel, Applied Acoustics 174 (2021) 107735.
22. H. Shao, J. He, J. Zhu, G. Chen, H. He: Low-frequency sound absorption of a tunable multilayer composite structure, Journal of Vibration and Control 28, 17–18 (2022) 2279–2287.
23. L. Yuvaraj, S. Jeyanthi, Acoustic performance of countersunk micro-perforated panel in multilayer porous material, Building Acoustics 27, 1 (2019) 3–20.
24. J. Carbajo, S.G. Mosanenzadeh, S. Kim, N.X. Fang: Multilayer perforated panel absorbers with oblique perforations, Applied Acoustics 169 (2020) 107496.
25. W. Yang, X. Bai, W. Zhu, R. Kiran, J. An, C.K. Chua, K. Zhou: 3D printing of polymeric multi-layer micro-perforated panels for tunable wideband sound absorption, Polymers 12 (2020) 360.
26. D. Li, D. Chang, B. Liu, J. Tian: Improving sound absorption bandwidth of micro-perforated panel by adding porous materials, INTER-NOISE and NOISE-CON Congress and Conference Proceedings 249 (2014) 6.
27. M. Rusli, F. Rahman, H. Dahlan, G. Bur, M. Bur: Sound absorption characteristics of a single micro-perforated panel backed by a natural fiber absorber material, Solid State Phenomena 307 (2020) 291–296.
28. Y. Wang, C. Zhang, L. Ren, M. Ichchou, M.-A. Galland, O. Bareille: Sound absorption of a new bionic multi-layer absorber, Composite Structures 108 (2014) 400–408.
29. Z. Liu, J. Zhan, M. Fard, J.L. Davy: Acoustic properties of a porous polycarbonate material produced by additive manufacturing, Material Letters 181 (2016) 296–299.
30. D.C. Akiwate, M.D. Date, B. Venkatesham, S. Suryakumur: Acoustic properties of additive manufactured narrow tube periodic structures, Applied Acoustics 136 (2018) 123–131.
31. D.C. Akiwate, M.D. Date, B. Venkatesham, S. Simhambhatla: Acoustic properties of additive manufactured porous material, in: M. Singh, Y. Rafat (Eds.), Recent developments in acoustics, Springer, Singapore, 2021, pp. 129–138.
32. T. Yamamoto, Y. Imae, Multi-scale analysis for sound absorption media by using microscopically periodic poroelastic material made by 3D printer, in: The 22nd International Congress on Sound and Vibration, , Florence, Italy, 12–16 July 2015.

33. X. Cai, J. Yang, G. Hu: Sound absorption by acoustic microlattice with optimized pore configuration, Journal of the Acoustical Society of America 144, 2, (2018) EL138–EL143.
34. M.D. Guild, C.A. Rohde, M.C. Rothko, C.F. Sieck: 3D printed acoustic metamaterial sound absorber using functionally-graded sonic crystals, European Acoustics Association, Crete, 2018.
35. T. Ring, S. Kuschmitz, H. Watschke, T. Vietor, S.C. Langer: Additive Fertigung und Charakterisierung akustisch wirksamer Materialien, in: Jahrestagung für Akustik DAGA2018, München, 19–22 March, 2018.
36. D. Akiwate, M.S. Ranjan, B. Venkatesham, S. Simhambhatla, S. Suryakumar: Acoustic characterization of additive manufactured layered porous material, INTER-NOISE and NOISE-CON Congress and Conference Proceedings 259 (2019) 6.
37. E.R. Fotsing, A. Dubourg, A. Ross, J. Mardjono: Acoustic properties of a periodic micro-structures obtained by additive manufacturing, Applied Acoustics 148 (2019) 322–331.
38. J. Boulvert, T. Cavalieri, J. Costa-Baptista, L. Schwan, V. Romero-Garcia, G. Gabard, E.R. Fotsing, A. Ross, J. Mardjono, J.-P. Groby: Optimally graded porous material for broadband perfect absorption of sound, Journal of Applied Physics 126, 17 (2019) 175101.
39. M. Vasina, K. Monkova, P.P. Monka, D. Kozak, J. Tkac: Study of the sound absorption properties of 3D-printed open-porous ABS material structures, Polymers 125 (2020) 1062.
40. J. Carbajo, J.M. Molina-Jordá, L.P. Maiorano, N.X. Fang: Sound absorption of macro-perforated additively manufactured media, Applied Acoustics 182 (2021) 108204.
41. W. Johnston, B. Sharma: Additive manufacturing of fibrous sound absorbers, Additive Manufacturing 41 (2021) 101984.
42. B. Berchtenbreiter, S. Becker: Complex fluid properties of additively manufactured periodic lattice structures, in: Jahrestagung für Akustik – DAGA, , Wien and Online, 15–18 August 2021, pp. 116–119.
43. S. Deshmukh, H. Ronge, S. Ramamoorthy: Design of periodic foam structures for acoustical applications: concept, parametric study and experimental validation, Materials and Design 175 (2019) 107830.
44. K.C. Opiela, T. Zieliński: Adaption of the equivalent-fluid model to the additively manufactured acoustic porous materials, in: M. Ochmann, M. Vorländer, J. Fels (Eds.), Proceedings of the 23rd International Congress on Acoustics: Integrating 4th EAA Euroregio 2019, Aachen, Germany, 9–13 September 2019, Deutsche Gesellschaft für Akustik, Aachen, Germany, 2019, pp. 1216–1223.
45. X. Zhao, X. Fan: Enhancing low frequency sound absorption of micro-perforated panel absorbers by using mechanical impedance plates, Applied Acoustics 88 (2015) 123–128.
46. J.F. Allard, N. Atalla: Propagation of sound in porous media: modelling sound absorbing materials, 2nd edn.John Wiley & Sons, Chichester, 2009.
47. D.L. Johnson, J. Koplik, R. Dashen: Theory of dynamic permeability and tortuosity in fluid-saturated porous media, Journal of Fluid Mechanics 176 (1987) 379–402.
48. Y. Champoux, J.-F. Allard: Dynamic tortuosity and bulk modulus in air-saturated porous media, Journal of Applied Physics 70, 4 (1991) 1975–1979.
49. N. Atalla, F. Sgard: Modeling of perforated plates and screens using rigid frame porous models, Journal of Sound and Vibration 303, 1–2 (2007) 195–208.
50. T.G. Zieliński, F. Chevilotte, E. Deckers: Sound absorption of plates with micro-slits backed with air cavities: Analytical estimations, numerical calculations and experimental validations, Applied Acoustics 146 (2019) 261–279.
51. B. Berchtenbreiter: Double-Layer MPA mit additiv gefertigten porösen Absorbern, PhD thesis, Friedrich-Alexander-Universität Erlangen-Nürnberg, 2023.
52. D. Lafarge: Propagation du son dans les matériaux poreux à structure rigide saturés par un fluide viscothermique: Définition de paramétres géométriques, analogie electromagnétique, temps de relaxation, PhD thesis, Université du Maine Le Mans, 1993.
53. D. Lafarge, P. Lemarinier, J.F. Allard, V. Tarnow: Dynamic compressibility of air in porous structures at audible frequencies, Journal of the Acoustical Society of America 102, 4 (1997) 1995–2006.
54. M. Niskanen, J.-P. Groby, A. Duclos, O. Dazel, J.C. Le Roux, N. Poulain, T. Huttunen, T. Lähivaara: Deterministic and statistical characterization of rigid frame porous materials from impedance tube measurements, Journal of the Acoustical Society of America 142, 4 (2017) 2407–2418.
55. B.H. Song, J.S. Bolton: A transfer-matrix approach for estimating the characteristic impedance and wave numbers of limp and rigid porous materials, Journal of the Acoustical Society of America 107, 3 (2000) 1131–1152.
56. A. Schulz: Die akustischen Randbedingungen perforierter Wandauskleidungen in Strömungskanälen – Physikalische Modelle und Eduktion, PhD thesis, Technische Universität Berlin, 2019.
57. L. Cremer: Theorie der Luftschall-Dämpfung im Rechteckkanal mit schluckender Wand und das sich dabei ergebende höchste Dämfpungsmaß, Acustica 3, 2 (1953) 249–263.
58. The MathWorks: MATLAB mathematics, Version 2018a, 2018. Available at https://de.mathworks.com/help/gads/ga.html?searchHighlight=ga&s_tid=srchtitle_support_results_1_ga.

Cite this article as: Berchtenbreiter B. Renz A. & Becker S. 2024. The potential of additively manufactured porous absorbers in the design of multi-layer microperforated absorbers. Acta Acustica, **8**, 37.